

## Autoresonant generation of solitons in Bose-Einstein condensates by modulation of the interaction strength

A. G. Shagalov<sup>1,\*</sup> and L. Friedland<sup>2,†</sup>

<sup>1</sup>*Institute of Metal Physics, Ekaterinburg 620990, Russian Federation*

<sup>2</sup>*Racah Institute of Physics, The Hebrew University, Jerusalem 91904, Israel*



(Received 1 September 2023; accepted 5 December 2023; published 2 January 2024)

The autoresonant approach to generation of solitary structures in Bose-Einstein condensates by chirped frequency space-time modulation of the interaction strength is proposed. Both a spatially periodic case and a finite-size trap are studied numerically within a Gross-Pitaevskii equation. Weakly nonlinear theory of the process is developed in the spatially periodic case using Whitham's averaged variational principle. The theory also describes the threshold phenomenon setting the lowest bound on the amplitude of modulations of the interaction strength for autoresonant excitation.

DOI: [10.1103/PhysRevE.109.014201](https://doi.org/10.1103/PhysRevE.109.014201)

### I. INTRODUCTION

Magnetically or optically controlled Feshbach resonance is an effective method to manipulate scattering length in Bose-Einstein condensates (BECs) [1] allowing one to control matter-wave patterns [2]. A variety of new phenomena in soliton dynamics were observed using this approach, such as resonant splitting of solitons [3], trapping of solitons [4], emergence of dark solitons and trains [5,6], splitting of solitons under a sudden quench [7], splitting two-soliton complexes [8], emission of jets from a driven soliton [9], and many others.

Modern advances in optical Feshbach resonance demonstrated [10] precise temporal and spatial control of the scattering length, opening a possibility to manage nonlinear dynamics of the condensate. In this paper we present an approach based on autoresonance to generate and control dark and bright solitons and other coherent structures in BECs by space-time modulation of the interaction strength. Dark solitons comprise localized dips in density of a condensate with repulsive interaction of particles and were observed experimentally in Refs. [11,12]. In contrast, bright solitons were observed as humps in the density of condensates with attractive interaction of particles [13,14]. The simplest model to describe both types of solitons is the one-dimensional Gross-Pitaevskii (GP) equation [15] for elongated condensates with strong transverse confinement. In this case the GP equation is similar to the nonlinear Schrödinger equation (NLS) with the sign of the nonlinearity associates with repulsive or attractive interactions. The NLS equation has exact analytic solutions for both bright and dark solitons [16,17].

The autoresonance is a general phenomenon in nonlinear systems which involves a continuous self-phase-locking of a system with chirped frequency-driving perturbations [18]. As

the driving frequency varies in time, the autoresonant system performs evolution in its parameter space, frequently leading to excitation of nontrivial large-amplitude states. It was shown in Ref. [19] that the autoresonance of a driven BEC can occur when the interaction strength oscillates in time, leading to oscillations of the width of the condensate as its frequency followed the slowly varying driving frequency.

The basic model for studying nonlinear dynamics of BECs is the GP equation [15] written in the dimensionless form

$$i\varphi_t + \varphi_{xx} - \mathbf{U}(x, t)\varphi + g(x, t)|\varphi|^2\varphi = 0. \quad (1)$$

Here time is measured in units of inverse transverse trapping frequency  $\omega_{\perp}^{-1}$  and space and density in units of  $l_{\perp} = [\hbar/(2m\omega_{\perp})]^{1/2}$  and  $m\omega_{\perp}/2\pi\hbar|a_0|$ , respectively, where  $m$  is the atomic mass. In Eq. (1),  $g = 2a(x, t)/|a_0|$  is the normalized, space-time modulated interaction strength, where  $a$  is the s-wave scattering length of interacting particles in the BEC. For condensates with repulsive interactions of particles  $a < 0$  and  $a > 0$  for attractive interactions. We assume that the modulation of  $a$  is small compared to the unperturbed scattering length  $a_0$  and can be controlled by the external magnetic field, for example. The form of the longitudinal trapping potential  $U(x)$  will be discussed in Sec. IV. A similar model appears in nonlinear optics [20,21] with the management of the nonlinear refractive index. Autoresonant excitation of dark GP solitons using parametric driving via space-time modulations of the trapping potential  $\mathbf{U}$  (the linear term in the GP equation) was discussed recently [22]. In contrast, in the present work we will exploit modulations of the interaction strength  $g$ . As mentioned above, managing the interaction strength is a promising recent tool for controlling BEC dynamics. We will analyze formation of autoresonant dark and bright GP solitons using this method, develop weakly nonlinear theory of the process, and study excitation and control of a two-phase GP solution, via chirped frequency standing wave-type perturbation of the interaction strength. The presentation will be as follows. Section II will focus on the spatially periodic domain case (for  $\mathbf{U} = 0$ ) and illustrate in simulations the formation of traveling

\*shagalov@imp.uran.ru

†lazar@mail.huji.ac.il

dark solitons, as well as excitation of two-phase solutions of the GP equation. In Sec. III we will develop a weakly nonlinear theory of these autoresonant excitations using Whitham’s averaged variational approach [23]. This approach is based on averaging the Lagrangian density associated with Eq. (1) over the fast space-time oscillations of the driven solution to extract the slow autoresonant evolution part of the problem via the averaged Lagrangian. Section IV will discuss the case of a finite BEC trap [U = U(x)]. Finally, Sec. V will present our conclusions.

**II. PERIODIC BOUNDARY CONDITIONS**

The case of periodic boundary conditions is usually analyzed in numerical simulations of an infinite domain for a spatially periodic driving. It is also used in 1D modeling along the torus-like BEC (ring-trap geometry) [24,25].

We set U = 0 in this case and assume the space-time dependent interaction strength

$$g(x, t) = 2\sigma\{1 + \varepsilon \cos[kx - \psi(t)]\}, \tag{2}$$

where  $\sigma = \pm 1$  and  $\varepsilon \ll 1$  is a small parameter. In the driving perturbation, we assume  $\psi(t) = \int \omega_d(t) dt$ , where the driving frequency  $\omega_d(t)$  slowly varies in time,  $\omega_d(t) = \omega_0 - \alpha t$ . We also assume that  $k$  is constant and given by boundary conditions ( $2\pi$  over the length of a circular trap, for example).

In the periodic case, when potential U = 0, the unperturbed ground state is the spatially homogeneous solution of Eq. (1)

$$\varphi(x, t) = U_0 e^{2i\sigma U_0^2 t} \tag{3}$$

with constant amplitude  $|\varphi| = U_0$ .

The frequency of a perturbed homogeneous state is [26,27]

$$\omega_0 = k\sqrt{k^2 - 4\sigma U_0^2}. \tag{4}$$

Condensates with repulsive interaction of particles when  $\sigma = -1$  are stable. In this case frequency (4) is known as the Bogolubov frequency. The dark solitons are typical structures in these condensates. In the opposite case ( $\sigma = 1$ ) bright solitons exist. In this case  $\omega_0$  can be imaginary, leading to modulational instability. This instability is well known in plasma physics and nonlinear optics [28,29]. If a condensate has length  $l$ , then the wave number of the main mode is  $k = 2\pi/l$  and the condition for stability restricts the density of the condensate,  $U_0^2 < \pi^2/l^2$ . If the condensate has a cigar-like shape with the transverse dimension  $l_\perp$ , then, in physical variables, the stability condition can be written as the restriction on the number of particles,  $n < (l_\perp/l)(l_\perp/a_0)$ . Nevertheless, the modulational instability does not prevent existence of bright solitons as demonstrated in experiments [13,14]. Furthermore, trains of bright solitons were formed as the result of the modulational instability [30,31].

In the numerical simulations below, we consider the case  $\sigma = -1$  first and start from the ground state (3), switch on the driving perturbation at  $t = t_0 < 0$ , and slowly chirp the driving frequency  $\omega_d(t)$  passing  $\omega_0$  at  $t = 0$ . One finds that after passage through this resonance, the system may evolve in two different ways. If the driving amplitude  $\varepsilon$  is small, the nonlinear shift of the eigenfrequency destroys the resonance and the excited wave amplitude saturates at a small level.

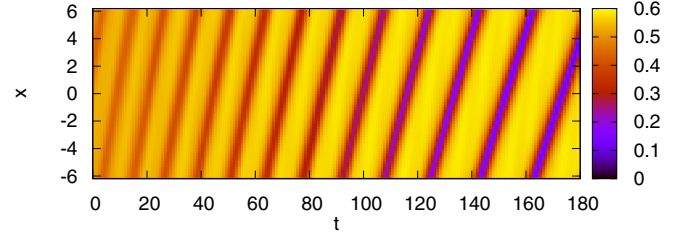


FIG. 1. Space-time color map of the dark soliton generation in periodic domain  $[-2\pi, 2\pi]$ . Driving parameters are  $\varepsilon = 0.03$ ,  $\alpha = 0.0015$ ,  $k = 0.5$ ,  $\omega_0 = 0.559$ , and  $t_0 = -200$

However, if  $\varepsilon$  exceeds a sharp threshold  $\varepsilon_{th}$  [see Eq. (31) in Sec. III], the phase of the excited solution locks to that of the drive and the system remains in resonance for a long time, resulting in excitation of a large-amplitude structure. This continuous phase-locking (autoresonance) effect can be used for generation of dark solitons, which are typical nonlinear structures in BECs for  $\sigma = -1$ . The theory of the threshold phenomenon will be developed in the next section.

The process of autoresonant generation of a dark soliton for  $\varepsilon > \varepsilon_{th}$  is illustrated by the example in Fig. 1 in a color map and, in more detail, in series of time frames of the amplitude and phase of the soliton shown in Fig. 2. The soliton moves to the right, increasing its amplitude and decreasing the velocity. The soliton velocity was calculated by following the motion of the minimum of the solitary structure in time. It has the direction and approximately the value of the phase velocity of the driving wave  $V_p = \omega_d(t)/k$  (see Fig. 3), illustrating the autoresonant phase synchronization between the generated soliton and the drive. The oscillating modulations of the

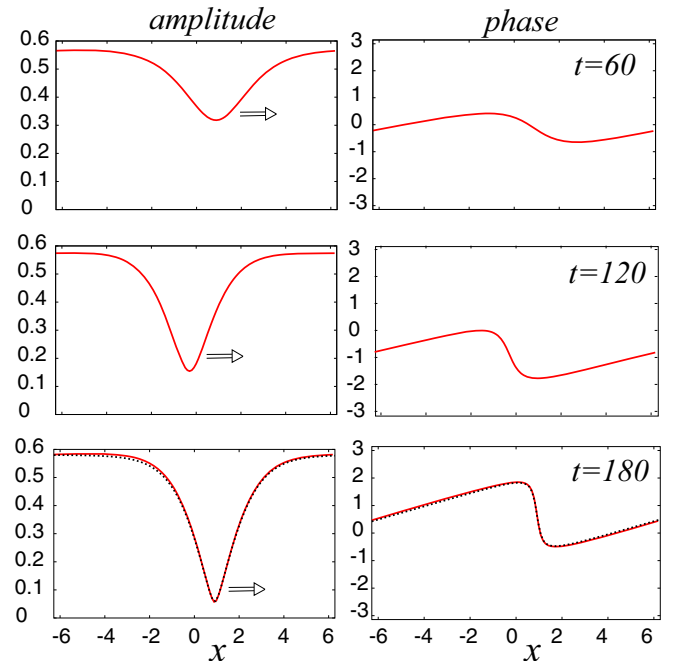


FIG. 2. Time frames of amplitude and phase of the soliton generation in Fig. 1. Dotted lines at  $t = 180$  are dark soliton solutions (A1) and (A2) for  $U_0 = 0.58$ ,  $\kappa = 0.24$ , and  $b = 0.995$ .

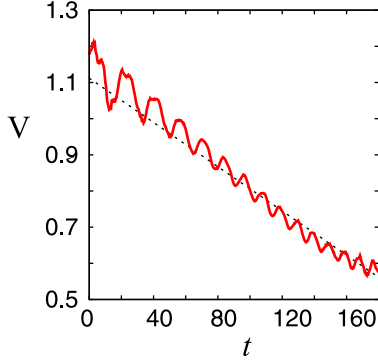


FIG. 3. Soliton velocity in numerical simulations (full red line) and the phase velocity of the driving wave  $V_p = \omega(t)/k$  (dotted line).

soliton velocity are due to the characteristic to autoresonance oscillations of the phase mismatch between the driving and the driven structures (see Sec. III A for more details).

We have also compared the numerically generated solution in Fig. 2 at  $t = 180$  with the analytic formulas (the dotted lines) describing dark solitons in the Appendix. One can see a very good agreement between the two. The soliton velocity given by Eq. (A3) is 0.595, which is also close to the velocity 0.585 found numerically at  $t = 180$ . This confirms that the autoresonantly excited *large-amplitude* waves, despite being formed on a finite support  $2\pi/k$ , are close to the usual soliton solutions. Note that the generated soliton moves to the right at all times because  $\kappa > 0$  and  $s > 0$  [see Eq. (A3)].

In several applications, in contrast to the traveling wave perturbations of the interaction strength discussed above, standing spatial drivings were used to control matter-wave patterns [2], for splitting soliton complexes [8], and in studying parabolically trapped BECs [32]. At this stage, we also apply a standing wave-type driving perturbation

$$g(x, t) = 2\sigma \{1 + \varepsilon \sin(kx) \sin[\psi(t)]\}. \quad (5)$$

This is a linear superposition of two modulations (2) with opposite phase velocities:  $\sin(kx) \sin(\psi) = (1/2)[\cos(kx - \psi) - \cos(kx + \psi)]$ . In this case, we expect formation of a two-phase solution  $\varphi(\theta_1, \theta_2)$ ,  $\theta_{1,2}$  being the phases of the two driving traveling waves. A weakly nonlinear theory of such excitations is presented in the second subsection of Sec. III. Transition to autoresonance in this case also requires the driving amplitude to exceed a sharp threshold [see Eq. (51)]. This result is in a good agreement with numerical simulations, as shown in Fig. 4. The circles in the figure correspond to numerical results such that for  $\varepsilon$  below these values the autoresonant synchronization between the driven and driving phases was lost (similar to the case shown in the right panel in Fig. 6 below). Autoresonant generation of two-phase solutions using a standing wave drive (5) is illustrated by the example in Fig. 5. Initially, formation of two small amplitude solitons moving with opposite velocities was observed, each associated with one of the traveling waves composing the standing wave drive. As the amplitude of the solitons increases, their velocities decrease and one of the resulting solitons is located near the center and another one near the boundary. The final solution has a large amplitude and small mobility. The next

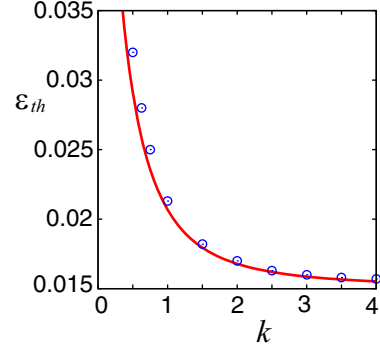


FIG. 4. Comparison of the theoretical threshold (51) (red line) with numerical simulations (circles) for  $U_0 = 0.5$  and  $\alpha = 0.001$ .

section presents the theory of such single- and two-phase autoresonant excitations.

### III. WEAKLY NONLINEAR THEORY

#### A. Traveling wave drive and the threshold phenomenon

Here we develop a weakly nonlinear theory of the autoresonance via modulation of the interaction strength within Gross-Pitaevskii (GP) equation [15] focusing on the  $U(x) = 0$  case for the traveling wave modulation described in Sec. II. The standing wave-type drive will be discussed in the next subsection. We proceed from GP equation

$$i\varphi_t + \varphi_{xx} + 2\sigma|\varphi|^2\varphi = -2\sigma\varepsilon|\varphi|^2\varphi \cos(kx - \psi) \quad (6)$$

and seek a solution of form  $\varphi = U \exp(iV)$  governed by the following set of real equations

$$U_t + V_{xx}U + 2V_xU_x = 0, \quad (7)$$

$$V_tU - U_{xx} + V_x^2U - 2\sigma U^3 = 2\sigma\varepsilon U^3 \cos(kx - \psi). \quad (8)$$

The Lagrangian density for this problem is

$$L = \frac{1}{2} [U_x^2 + U^2(V_x^2 + V_t)] - \frac{\sigma}{2} U^4 - \sigma\varepsilon \frac{U^4}{2} \cos(kx - \psi). \quad (9)$$

The Lagrangian representation suggests using Whitham's averaged variational approach [23] in analyzing our problem, similar to the direct driving case studied previously [27]. The first step in this direction is to assume constant frequency

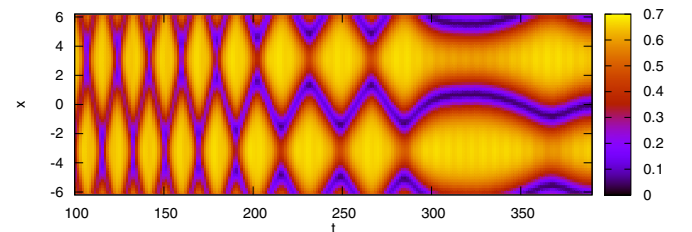


FIG. 5. Space-time color map of solitons generation on periodic domain  $[-2\pi, 2\pi]$  with a standing wave drive. Parameters of the driving:  $\varepsilon = 0.06$ ,  $\alpha = 0.0015$ ,  $k = 0.5$ ,  $\omega_0 = 0.559$ ,  $t_0 = -200$ .

drive,  $\psi = \omega_d t$ , and seek solutions of the linearized problem of form

$$U = U_0 + u_1 \cos(kx - \psi), \quad (10)$$

$$V = 2\sigma U_0^2 t + v_1 \sin(kx - \psi), \quad (11)$$

[Note that our unperturbed solution is  $\varphi_0 = U_0 \exp(2i\sigma U_0^2 t)$ . Then by linearization, Eqs. (7) and (8) yield

$$\omega_d u_1 - k^2 U_0 v_1 = 0, \quad (12)$$

$$-\omega_d v_1 U_0 + (k^2 - 4\sigma U_0^2) u_1 = \frac{1}{2} \varepsilon \sigma U_0^3, \quad (13)$$

i.e.,

$$v_1 = -\frac{\varepsilon \sigma \omega_d U_0^2}{2(\omega_d^2 - \omega_0^2)}, \quad (14)$$

$$u_1 = \frac{k^2 U_0}{\omega_d} v_1, \quad (15)$$

where the linear resonance frequency  $\omega_0 = k\sqrt{k^2 - 4\sigma U_0^2}$ . Next, we proceed to chirped-driven problem, where  $\psi = \int \omega_d(t) dt$ , and extend Eqs. (10) and (11) to next nonlinear order

$$U = U_0 + u_1 \cos \theta + [u_0 + u_{11} \cos(2\theta)], \quad (16)$$

$$V = 2\sigma U_0 t + v_1 \sin \theta + [\xi + v_{11} \sin(2\theta)]. \quad (17)$$

Here  $u_1$  and  $v_1$  are small (viewed as first-order perturbations), while all the terms in the square brackets are assumed to be of second order in  $u_1$  and  $v_1$ . In these solutions  $\theta = kx - \phi$  and  $\phi = \int \omega(t) dt$  is an additional independent variable. Furthermore, all the amplitudes are now assumed to be slowly varying functions of time. The reason for choosing the second-order ansatz of this form is consistent with the form of the Lagrangian density containing either different powers of  $U$  or products of derivatives of  $V$  and powers of  $U$ . The auxiliary phase  $\xi = \int \gamma(t) dt$  in Eq. (17) is necessary because  $V$  is the potential (it enters the Lagrangian density via derivatives only [23]).

The next step is to replace  $\psi = \phi + \Phi$  in the driving part of the Lagrangian density and substitute the above ansatz into the Lagrangian density (9) and average it over  $\phi \in [0, 2\pi]$  and  $x \in [0, 2\pi/k]$ . This averaging and all algebra here and below are done via *Mathematica*. The resulting averaged Lagrangian density is

$$\begin{aligned} \Lambda = & A + \frac{\gamma}{2} U_0^2 - \frac{3}{16} \sigma u_1^4 + B v_1^2 + C v_1 u_1 + D u_1^2 \\ & + E u_1^2 v_1^2 + F - \sigma \varepsilon U_0^3 u_1 \cos \Phi, \end{aligned} \quad (18)$$

where

$$A = \frac{1}{4} [-2U_0 u_1 (2\sigma U_0 u_1 + \omega v_1) + k^2 (u_1^2 + U_0^2 v_1^2)],$$

$$B = \frac{k^2 U_0}{4} (2u_0 + u_{11}),$$

$$C = -\frac{1}{4} (2\omega u_0 + \omega u_{11} - 4k^2 U_0 v_{11}),$$

$$D = \frac{1}{4} (\gamma - 12\sigma u_0 U_0 - 6\sigma U_0 u_{11} - \omega v_{11}),$$

$$E = \frac{3}{16} k^2,$$

$$\begin{aligned} F = & \gamma u_0 U_0 - 2\sigma u_0^2 U_0^2 + (k^2 - \sigma U_0^2) u_1^2 \\ & - \omega U_0 u_{11} v_{11} + k^2 U_0^2 v_{11}^2. \end{aligned}$$

Note that the term  $A$  in  $\Lambda$  is quadratic in the amplitudes and thus describes the linear part of the problem. Furthermore, the averaged Lagrangian density  $\Lambda = \Lambda_{\text{tr}}(u_1, v_1, u_0, u_{11}, v_{11}; \omega, \gamma, \Phi)$  is a function of all five slowly varying amplitudes and two phases  $\phi$  and  $\xi$  entering via their time derivatives  $\omega = d\phi/dt$  and  $\gamma = d\xi/dt$  and the phase mismatch  $\Phi = \psi - \phi$  in the driving term.

The next step is taking variations with respect to second-order amplitudes  $u_{11}, v_{11}$ , resulting in two equations  $\partial \Lambda_{\text{tr}} / \partial u_{11} = 0$  and  $\partial \Lambda_{\text{tr}} / \partial v_{11} = 0$ . To lowest significant order in solving these equations, we replace  $v_1$  by its linear approximation  $v_{10} = \frac{\omega_0}{k^2 U_0} u_1$  [see Eq. (15)], where being interested in the vicinity of the resonance we also replaced  $\omega_d$  by the linear resonance frequency  $\omega_0$ . The resulting solutions are

$$u_{11} = -\frac{1}{4U_0} + \frac{2\sigma U_0}{k^2} u_1^2, \quad (19)$$

$$v_{11} = -\frac{\omega_0 (k^2 - 2\sigma U_0^2)}{2k^4 U_0^2} u_1^2. \quad (20)$$

Similarly, variations with respect to  $u_0$  and  $\xi$  yield equations  $\partial \Lambda_{\text{tr}} / \partial u_0 = 0$  and  $d(\partial \Lambda_{\text{tr}} / \partial \gamma) / dt = 0$ , and corresponding solutions

$$u_0 = -\frac{u_1^2}{4U_0}, \quad \gamma = 2\sigma u_1^2. \quad (21)$$

Furthermore, the variation with respect to  $\phi$  yields the equation

$$\frac{d}{dt} \left( \frac{\partial \Lambda_{\text{tr}}}{\partial \omega} \right) = \frac{\partial \Lambda_{\text{tr}}}{\partial \Phi} \quad (22)$$

or

$$\frac{du_1}{dt} = \sigma \varepsilon \frac{k^2 U_0^3}{\omega_0} \sin \Phi. \quad (23)$$

The last two reduction steps are varying with respect to  $v_1$  and  $u_1$ . As before, in all these developments, we replace  $v_1$  by  $v_{10}$  and  $\omega$  by  $\omega_0$  in higher than first-order terms. Then the variation with respect to  $v_1$  yields the expression

$$v_1 = \frac{\omega}{k^2 U_0} u_1 + \frac{\omega_0 (5k^2 - 24\sigma U_0^2)}{8k^4 U_0^3} u_1^3. \quad (24)$$

Finally, the variation with respect to  $u_1$  after substitution of the last expression for  $v_1$  results in the following equation:

$$\omega_0^2 - \omega^2 = -8\sigma (k^2 - 3\sigma U_0^2) u_1^2 + \varepsilon \sigma \frac{2k^2 U_0^3}{u_1} \cos \Phi. \quad (25)$$

This allows us to approximate  $\omega$  near the Bogolubov frequency

$$\omega \approx \omega_0 + \frac{4\sigma (k^2 - 3\sigma U_0^2)}{\omega_0} u_1^2 - \varepsilon \sigma \frac{k^2 U_0^3}{\omega_0 u_1} \cos \Phi \quad (26)$$

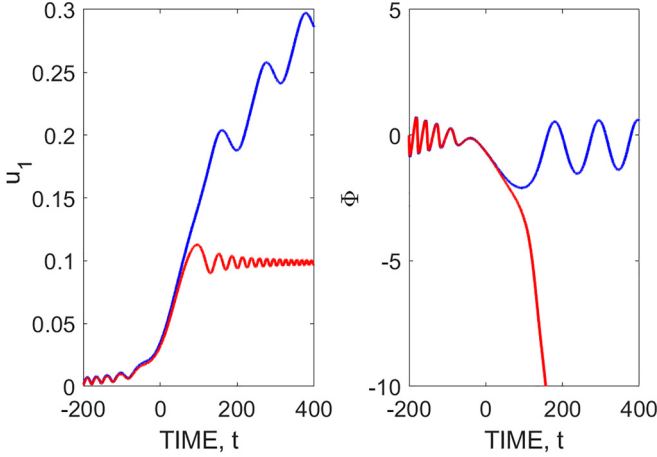


FIG. 6. Amplitude  $u_1$  of weakly nonlinear oscillations of  $U$  (left panel) and phase mismatch  $\Phi$  (right panel) vs time for  $\varepsilon$  5% below (red lines) and 5% above (blue lines) the threshold value of 0.021. The parameters are  $\sigma = -1$ ,  $U_0 = 0.5$ ,  $\alpha = 0.0015$ ,  $k = 0.5$ .

and write the equation describing the evolution of the phase mismatch

$$\frac{d\Phi}{dt} = \omega_d - \omega = -\alpha t - \sigma N u_1^2 + \varepsilon \sigma \frac{k^2 U_0^3}{\omega_0 u_1} \cos \Phi, \quad (27)$$

where

$$N = \frac{4(k^2 - 3\sigma U_0^2)}{\omega_0} = \frac{k^2}{\omega_0} + 3 \frac{\omega_0}{k^2}. \quad (28)$$

Equations (23) and (27) comprise a complete set describing the autoresonance in the problem. These equations can be put in a more concise form by introducing slow dimensionless time  $\tau = t/\sqrt{|\alpha|}$  and introducing a new complex variable  $\Psi = A e^{i\Phi}$ , where  $A = \frac{\sqrt{|N|}}{|\alpha|^{1/4}} u_1$ :

$$i \frac{d\Psi}{dt} + [-\text{sgn}(\alpha)\tau + \sigma|\Psi|^2]\Psi = \mu, \quad (29)$$

where

$$\mu = \varepsilon \frac{k^2 U_0^3 \sqrt{|N|}}{\omega_0 |\alpha|^{3/4}}. \quad (30)$$

This single-parameter equation is characteristic of autoresonant phenomena and yields a sharp threshold  $\mu_{\text{th}} = 0.41$  [18] for transition to autoresonance when starting from  $\Psi = 0$  at sufficiently large negative times. This can be transformed to the threshold on the driving amplitude

$$\varepsilon_{\text{th}} = 0.41 \frac{\omega_0 |\alpha|^{3/4}}{k^2 U_0^3 \sqrt{|N_{\text{tr}}|}} = 0.41 \frac{|\alpha|^{3/4}}{U_0^3 \sqrt{\frac{k^6}{\omega_0^3} + 3 \frac{k^2}{\omega_0}}}. \quad (31)$$

We illustrate this transition to autoresonance for the traveling wave drive in the case  $U_0 = 0.5$ ,  $k = 0.5$ ,  $\sigma = -1$ , and  $\alpha = -0.003$  ( $\varepsilon_{\text{th}} = 0.021$ ) in Fig. 6 showing the evolution of  $u_1$  (left panel) and  $\Phi$  (right panel) for  $\varepsilon$  being 5% below (red lines) and 5% above (blue lines) the threshold. One can see a continuing growth of  $u_1$  and phase locking of  $\Phi$  near zero above the threshold. Figure 7 shows the space-time evolution of the weakly nonlinear solution for

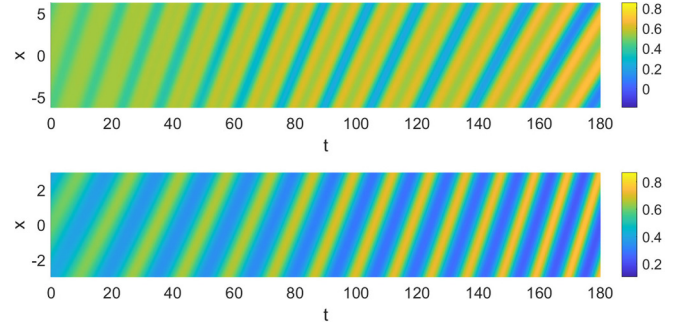


FIG. 7. Solution  $U$  in space-time from Eq. (16). The upper panel shows growing amplitude traveling dark soliton for parameters  $\sigma = -1$ ,  $U_0 = 0.5$ ,  $k = 0.5$ ,  $\alpha = 0.0015$ ,  $\varepsilon = 0.03$ . The lower panel illustrates growing amplitude bright soliton for parameters  $\sigma = 1$ ,  $U_0 = 0.5$ ,  $k = 1.05$ ,  $\alpha = -0.0015$ ,  $\varepsilon = 0.01$ . In both panels the  $x$  axis is over the periodicity interval of  $2\pi/k$ .

$U$  [see Eq. (16)]. The upper panel shows a growing amplitude traveling dark soliton for the same parameters as in the full simulations illustrated in Fig. 1 ( $\sigma = -1$ ,  $U_0 = 0.5$ ,  $k = 0.5$ ,  $\alpha = 0.0015$ ,  $\varepsilon = 0.03$ ). The lower panel illustrates a growing amplitude bright soliton for parameters  $\sigma = 1$ ,  $U_0 = 0.5$ ,  $k = 1.05$ ,  $\alpha = -0.0015$ ,  $\varepsilon = 0.01$ . Note that the sign of the driving frequency chirp rate was reversed in the latter case because of the change of sign of the nonlinear term in the GP equation.

## B. Standing wave drive

Here we analyze the case of the standing wave drive, i.e., discuss the driven GP equation of the form

$$i\varphi_t + \varphi_{xx} + 2\sigma|\varphi|^2\varphi = -2\sigma\varepsilon|\varphi|^2\varphi \sin(kx) \sin \psi. \quad (32)$$

As before, we seek a solution  $\varphi = U \exp(iV)$  governed by the following set of real equations:

$$U_t + V_{xx}U + 2V_x U_x = 0, \quad (33)$$

$$V_t U - U_{xx} + V_x^2 U - 2\sigma U^3 = 2\sigma\varepsilon U^3 \sin(kx) \sin \psi. \quad (34)$$

The Lagrangian density for this problem is

$$L = \frac{1}{2} [U_x^2 + U^2 (V_x^2 + V_t)] - \frac{\sigma}{2} U^4 - \sigma\varepsilon \frac{U^4}{2} \sin(kx) \sin \psi. \quad (35)$$

The analysis below is very similar to that for the traveling wave drive. Despite increased algebraic complexity it will pass all the steps described above, relying again on the *Mathematica* package, but only the main details will be presented below. We start by assuming a constant frequency drive  $\psi = \omega_d t$  and consider the linearized problem with solutions of the form

$$U = U_0 + u_1 \sin(kx) \sin \psi, \quad (36)$$

$$V = 2\sigma U_0^2 t + v_1 \sin(kx) \cos \psi, \quad (37)$$

yielding linear amplitudes [compare to Eqs. (14) and (15) in the traveling wave case]

$$v_1 = -\frac{2\varepsilon\sigma\omega_d U_0^2}{\omega_d^2 - \omega_0^2}, \quad (38)$$

$$u_1 = \frac{k^2 U_0}{\omega_d} v_1. \quad (39)$$

We observe that these linear solutions are a superposition of two independent traveling waves propagating in opposite directions and driven by the corresponding traveling wave components comprising the drive:

$$U = U_0 + \frac{u_1}{2}(\cos\theta_1 - \cos\theta_2), \quad (40)$$

$$V = 2\sigma U_0^2 t + \frac{v_1}{2}(\sin\theta_1 + \sin\theta_2), \quad (41)$$

where  $\theta_1 = kx - \phi$  and  $\theta_2 = kx + \phi$ , where  $\phi$  is a new independent variable. These solutions suggest the following higher order extension:

$$U = U_0 + \frac{u_1}{2}(\cos\theta_1 - \cos\theta_2) + [u_0 + u_{11} \cos(2\theta_1) + u_{22} \cos(2\theta_2) + u_{12}^+ \cos(\theta_1 + \theta_2) + u_{12}^- \cos(\theta_1 - \theta_2)], \quad (42)$$

$$V = 2\sigma U_0 t + \frac{v_1}{2}(\sin\theta_1 + \sin\theta_2) + [\xi + v_{11} \sin(2\theta_1) + v_{22} \sin(2\theta_2) + v_{12}^+ \cos(\theta_1 + \theta_2) + v_{12}^- \sin(\theta_1 - \theta_2)], \quad (43)$$

where  $\xi = \int \gamma dt$ , all the terms in square parentheses are of second order in  $u_1$  and  $v_1$ , while all the amplitudes are assumed to be slowly varying functions of time. The reason for choosing the second-order ansatz of this form is consistent with the form of the Lagrangian as described in the previous subsection.

The next step is to write  $\psi = \phi + \Phi$ , to substitute the ansatz (42) and (43) in the Lagrangian density  $L$ , and to average  $L$  over  $\phi \in [0, 2\pi]$  and  $x \in [0, 2\pi/k]$ . This yields the averaged Lagrangian density

$$\Lambda(u_1, v_1, u_0, u_{11}, u_{22}, u_{12}^+, u_{12}^-, v_{11}, v_{22}, v_{12}^+, v_{12}^-; \omega, \gamma, \Phi) \quad (44)$$

as a function of 11 slowly varying amplitudes and two phases  $\phi$  and  $\xi$  entering via their time derivatives  $\omega = d\phi/dt$  and  $\gamma = d\xi/dt$  and the phase mismatch  $\Phi = \psi - \phi$  in the driving term. Similar to the traveling wave drive, taking variations using  $\Lambda$  with respect to all higher order amplitudes  $u_0, u_{11}, u_{22}, u_{12}^+, u_{12}^-, v_{11}, v_{22}, v_{12}^+, v_{12}^-$  and  $\xi$  yield solutions

$$\begin{aligned} u_0 &= -u_1^2/(8U_0), \\ \gamma &= \sigma u_1^2, \\ u_{11} &= u_1^2(-1 + 8\sigma U_0^2/k^2)/(16U_0), \\ u_{22} &= u_{11}, \\ u_{12}^+ &= -u_1^2/(8U_0), \\ u_{12}^- &= -u_{12}^+, \\ v_{11} &= -\omega_0(k^2 - 2\sigma U_0^2)u_1^2/(8k^4 U_0^2), \end{aligned}$$

$$\begin{aligned} v_{22} &= -v_{11}, \\ v_{12}^+ &= 0, \\ v_{12}^- &= (k^2 - 2\sigma U_0^2)u_1^2/(4\omega_0 U_0^2). \end{aligned} \quad (45)$$

In finding these second-order solutions, we again replaced  $v_1$  by its linear approximation  $v_{10} = \frac{\omega_0}{k^2 U_0} u_1$ .

The next step is taking variation with respect to  $\phi$  yielding the same result as for the traveling drive case [see Eq. (23)]

$$\frac{du_1}{dt} = \sigma\varepsilon \frac{k^2 U_0^3}{\omega_0} \sin\Phi. \quad (46)$$

Next, as in the traveling drive case, we take variations with respect to  $v_1$  and find

$$v_1 = \frac{\omega}{k^2 U_0} u_1 + \frac{\omega_0(11k^2 - 24\sigma U_0^2)}{32k^4 U_0^3} u_1^3, \quad (47)$$

which differs from the traveling drive case [see Eq. (24)] by the coefficient in the nonlinear term. Finally, the variation with respect to  $u_1$  and substitution of  $v_1$  from Eq. (47) yields [compare to Eq. (24) for the traveling wave drive]

$$\omega^2 - \omega_0^2 = -3(-\sigma k^2 + 2U_0^2)u_1^2 - \varepsilon \frac{2\sigma k^2 U_0^3}{u_1} \cos\Phi. \quad (48)$$

As before, this result allows to obtain the evolution equation for the phase mismatch

$$\frac{d\Phi}{dt} = -\alpha t - \sigma N u_1^2 + \varepsilon \sigma \frac{k^2 U_0^3}{\omega_0 u_1} \cos\Phi, \quad (49)$$

where the nonlinear coefficient

$$N = \frac{3(k^2 - 2\sigma U_0^2)}{2\omega_0} = \frac{3}{4} \left( \frac{k^2}{\omega_0} + \frac{\omega_0}{k^2} \right). \quad (50)$$

Equations (46) and (49) comprise a full set for completing the solution of the weakly nonlinear problem and, as for the traveling drive, yield the threshold on the driving amplitude for transition to Feshbach autoresonance in the problem:

$$\varepsilon_{\text{th}} = 0.41 \frac{|\alpha|^{3/4}}{k^2 U_0^3 \sqrt{|N|}} = 0.41 \frac{|\alpha|^{3/4}}{U_0^3 \sqrt{\frac{3}{4} \left( \frac{k^6}{\omega_0^3} + \frac{k^2}{\omega_0} \right)}}. \quad (51)$$

We illustrate evolution of  $u_1$  and  $\Phi$  in the case of a standing wave drive in Fig. 8 for two sets of parameters:  $\sigma = -1$ ,  $U_0 = 0.5$ ,  $k = 0.5$ ,  $\alpha = 0.0015$  (blue solid lines) and  $\sigma = 1$ ,  $U_0 = 0.5$ ,  $k = 1.05$ ,  $\alpha = -0.0015$ , (dotted red lines) and  $\varepsilon = 1.05\varepsilon_{\text{th}}$  in both cases ( $\varepsilon_{\text{th}} = 0.039$  and  $0.046$  for  $\sigma = -1$  and  $\sigma = 1$ , respectively). Note that in  $\sigma = 1$  case in simulations, we start from a modulationally stable ground state (short-length or low-density condensates). One observes growing amplitude excitation (we are above the threshold in both cases) and phase locking of the phase mismatch near zero, indicating synchronization of the excitation with the drive. Figure 9 illustrates formation of a growing amplitude autoresonant solution  $U(x, t)$  in the weakly nonlinear model [see Eq. (42)] in the two cases shown in Fig. 8,  $\sigma = -1$  (upper panel) and  $+1$  (lower panel).

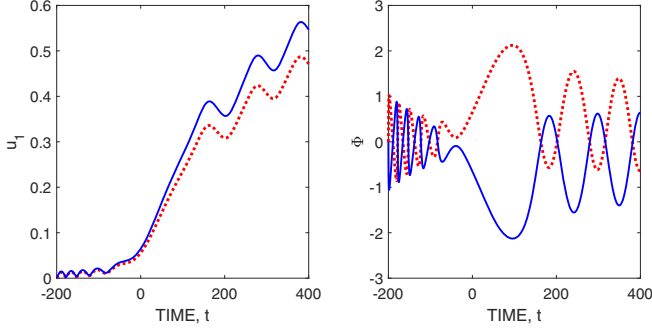


FIG. 8. Amplitude  $u_1$  (left panel) of oscillations of  $U$  and phase mismatch  $\Phi$  vs time for two sets of parameters: (blue lines)  $\sigma = -1$ ,  $U_0 = 0.5$ ,  $k = 0.5$ ,  $\alpha = 0.0015$ ,  $\varepsilon = 0.041$  ( $\varepsilon_{\text{th}} = 0.039$ ) and (red dotted lines)  $\sigma = 1$ ,  $U_0 = 0.5$ ,  $k = 1.05$ ,  $\alpha = -0.0015$ ,  $\varepsilon = 0.049$  ( $\varepsilon_{\text{th}} = 0.046$ ).

#### IV. FINITE TRAP

In this section we demonstrate in simulations that large-amplitude soliton-like structures can be generated via autoresonance in a finite domain case using a well-type potential  $\mathbf{U}(\mathbf{x})$ . Let us proceed from a standard harmonic potential  $\frac{1}{2}m\omega_{\parallel}^2x^2$ , which in the dimensionless form of Eq. (1) becomes  $\mathbf{U}(\mathbf{x}) = \gamma^2x^2$  where  $\gamma = \omega_{\parallel}/2\omega_{\perp}$ . In numerical simulations in this section, it is convenient to make additional rescaling of variables:  $t = \gamma^{-1}t'$ ,  $x = \gamma^{-1/2}x'$  and  $\varphi = \gamma^{1/2}\varphi'$ , which preserves the form of Eq. (1), but reduces  $\gamma$  to unity. In what follows, we will use an elongated well-type potential:  $\mathbf{U} = 0$  for  $-L < x < L$  and  $\mathbf{U} = (x - L)^2$  at  $x > L$ ,  $\mathbf{U} = (x + L)^2$  for  $x < -L$ , which yields the harmonic potential for  $L = 0$ . The ground state in potential  $\mathbf{U}(\mathbf{x})$  is inhomogeneous and comprises the eigenfunction of the stationary equation

$$\varphi_{0,xx} - \mathbf{U}(x)\varphi_0 + 2\sigma|\varphi_0|^2\varphi_0 = \Lambda\varphi_0, \quad (52)$$

as follows from Eq. (1) after substitution  $\varphi = \phi_0(x)\exp(i\Lambda t)$  in the unperturbed case,  $\varepsilon = 0$ . This is a nonlinear eigenstate parametrized by its amplitude  $\varphi_0(0)$ . The autoresonant driving will be applied to these states in the following. We consider case  $\sigma = -1$  first. The autoresonant generation of a soliton-like structure in simulations in this case in a finite trap

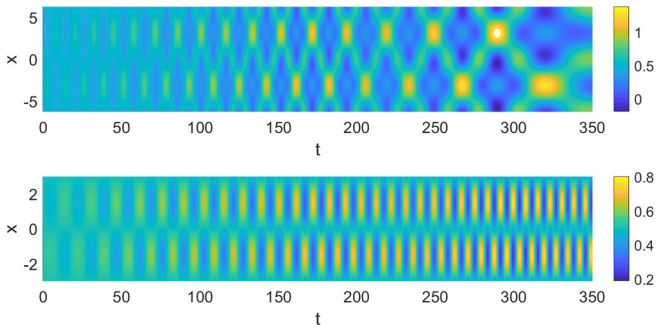


FIG. 9. Solution  $U$  in space-time in a weakly nonlinear model [see Eq. (42)] for the standing wave drive. The parameters are the same two sets as in Fig. 8:  $\sigma = -1$  (the upper panel) and  $\sigma = 1$  (the lower panel).

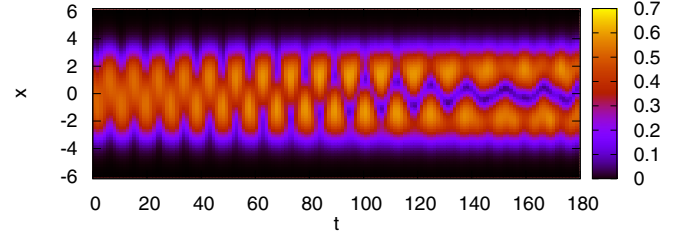


FIG. 10. Color map of generation of the dark soliton in the finite trap with  $L = 2$ ,  $\sigma = -1$ , parameters of the ground state,  $\varphi(0) = 0.5$ ,  $\Lambda = -0.602$ , and driving parameters,  $\varepsilon = 0.16$ ,  $\alpha = 0.0015$ ,  $k = 0.5$ ,  $\omega_0 = 0.7$ ,  $t_0 = -100$ .

for parameters  $L = 2$ ,  $\sigma = -1$ ,  $\varphi(0) = 0.5$ ,  $\Lambda = -0.602$ , and driving parameters  $\varepsilon = 0.16$ ,  $\alpha = 0.0015$ ,  $k = 0.5$ ,  $\omega_0 = 0.7$ ,  $t_0 = -100$  is illustrated by the space-time color map and in a series of time frames in Figs. 10 and 11. The initial ground state used in the simulations is shown in Fig. 11 by dotted lines. Initially a nucleated soliton has a small amplitude and oscillates in the trap many times increasing its amplitude. The final large-amplitude soliton also oscillates around the center of the trap. We observed that the width of the excited soliton is less than the width of the ground state and that the amplitude and phase of the excited waveform is similar to that of a dark soliton. We have also found in simulations that these excitations can be generated only if the trap is sufficiently wide,  $L > 0.25$  in our case. The width of our elongated potential can be estimated as  $\sqrt{2} + 2L$ . On the other hand, the width of a large-amplitude ( $b \approx 1$ ) soliton is  $1/\varphi_0(0)$ . For  $\varphi_0(0) = 0.5$ , used in the simulations, both widths are comparable for

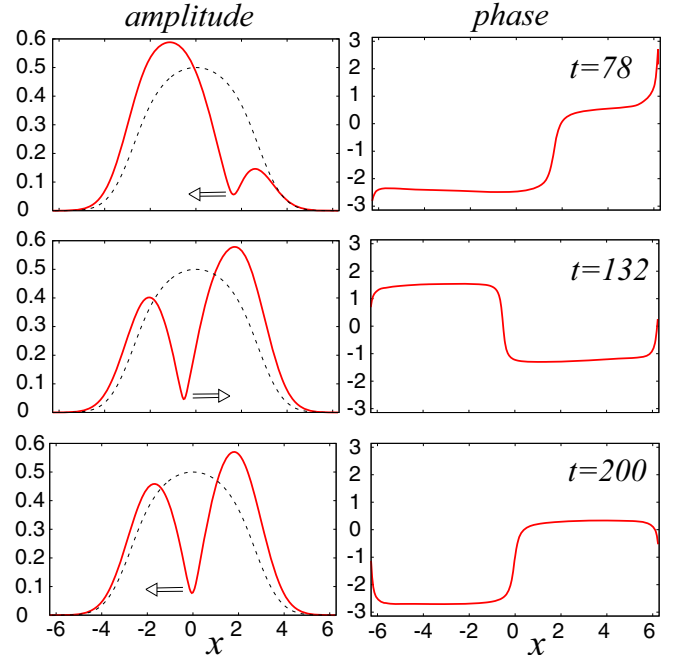


FIG. 11. Time frames of amplitude and phase of the soliton shown in Fig. 10. The dotted lines represent the amplitude of the ground state  $\varphi_0(x)$ . The arrows show the direction of motion of the solitons.

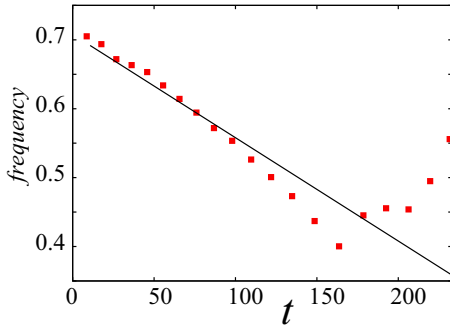


FIG. 12. Comparison of the soliton oscillation frequency (red squares) with the driving frequency (solid line) at parameters of Fig. 10.

$L \approx 0.25$ . Thus, we conclude that the autoresonant generation of dark solitons is possible in potentials having widths larger than that of the soliton. Using the physical parameters, the soliton width is  $\sqrt{2}\xi_h$ , where  $\xi_h = (8\pi a_0 |\varphi_0|^2)^{-1}$  is the healing length. Our simulations demonstrate a qualitative agreement with basic formulas describing dark solitons in the Appendix. At each time, the soliton has  $\kappa \approx 0$  and changes sign  $s$  according to the direction motion in agreement with Eq. (A3). One can see in Fig. 10 that the period of oscillations of the soliton inside the trap increases with time. This effect is due to the autoresonant synchronization with the drive as the driving frequency decreases in time ( $\alpha > 0$ ). We illustrate this synchronization in Fig. 12. One can see that the soliton oscillation frequency in the trap follows that of the drive for  $t < 120$ . Later, the frequencies start deviating, and above  $t = 150$  the synchronization is lost. In this off-resonance stage, the soliton freely oscillates around the center of the trap.

The problem of the modulational instability for  $\sigma = 1$  restricts the selection of the initial state for achieving autoresonant excitation. This state must be stable for a time longer than the typical autoresonant excitation time  $\sim 1/\sqrt{\alpha}$ . We focus on the simplest initial state with  $\varphi_0(x) > 0$  and having a single maximum  $\varphi_m = \varphi_0(0)$  at the center of the trap. For example, a steady bright soliton [16]  $\varphi_0(x) = \varphi_m / \cosh(\varphi_m x)$ ,  $\Lambda = \varphi_m$  for  $L \rightarrow \infty$ , is the initial state of this type. It is modulationally stable for all amplitudes. For finite  $L$  such a solution can be found numerically. For a given amplitude  $\varphi_m$  it decreases its width and the eigenvalue  $\Lambda$  conserving the soliton-like shape. In the previous section, such a soliton was generated autoresonantly from the homogeneous ground state which was modulationally stable for the sufficiently small length of the condensate. In a finite trap, such a scenario of soliton generation is impossible because of a rapid destruction of the homogeneous initial state, which is not a stationary solution of Eq. (52). The autoresonant excitation of the condensate in simulations with a soliton-type initial state is shown in Fig. 13 for  $\sigma = 1$  in a finite trap with  $L = 1$ . The parameters of the ground state are  $\varphi(0) = 1.0$ ,  $\Lambda = 0.883$  and the driving parameters are  $\varepsilon = 0.08$ ,  $\alpha = -0.0015$ ,  $k = 0.5$ ,  $\omega_0 = 0.67$ ,  $t_0 = -100$ . The soliton oscillates between the boundaries of the trap with the increasing frequency, following the driving frequency due to the autoresonant synchronization (see Fig. 14).

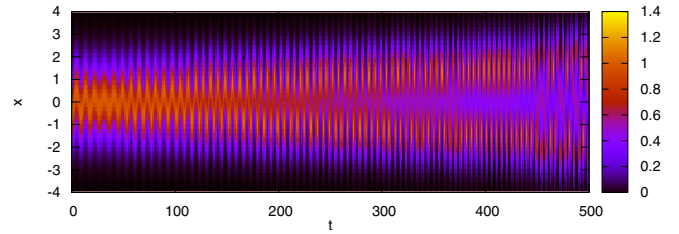


FIG. 13. Color map of autoresonant excitation of the condensate at  $\sigma = 1$  in the finite trap with  $L = 1$ . Parameters of the ground state:  $\varphi(0) = 1.0$ ,  $\Lambda = 0.883$ . Driving parameters:  $\varepsilon = 0.08$ ,  $\alpha = -0.0015$ ,  $k = 0.5$ ,  $\omega_0 = 0.67$ ,  $t_0 = -100$ .

## V. CONCLUSIONS

We have shown that a special type of space-time periodic modulations of the interaction strength allows one to generate and control large-amplitude solitons and other nonlinear structures of GP equation. Two simplest types of modulations, a traveling wave-like [see Eq. (2)] and a standing wave spatial pattern [see Eq. (5)], were analyzed subject to periodic boundary conditions or on a finite domain (a potential well-like trap). In both cases, the modulations of the interaction strength had small amplitudes and were frequency linearly chirped in time, crossing the Bogolubov frequency  $\omega_0$  of the ground state of the BEC. The Whitham's averaged variational principle [23] was used in developing a weakly nonlinear theory of the passage through  $\omega_0$  in the system and in finding the thresholds on the driving amplitudes of the modulations yielding autoresonant phase-locking. These thresholds scale with the chirp rate  $\alpha$  as  $\sim |\alpha|^{3/4}$  [see Eqs. (31) and (51)], which was confirmed in simulations in the periodic case. These numerical simulations demonstrated a continuous self-preservation (autoresonance) of the phase locking between the excited structure and the driving modulations after passage through resonance, resulting in the adiabatic excitation of large-amplitude solitary structures. In particular, we observed formation of traveling dark solitons moving with the velocity close to that of the traveling driving wave. For stable condensates ( $\sigma = -1$ ) one period of excited waveform can be extended periodically to elongated condensates forming a multisoliton train. In the case of a standing wave-type driving perturbation, two-phase nonlinear waveforms were generated,

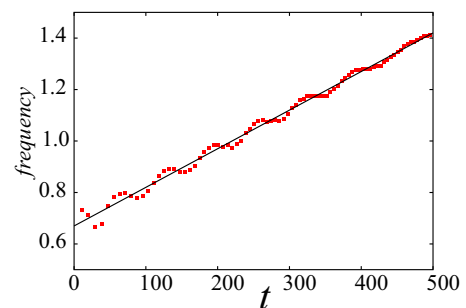


FIG. 14. Comparison of the soliton oscillation frequency (red squares) with the driving frequency (solid line) for parameters of Fig. 13.

which, in the final stage, slowed and became localized near the center and the boundary of the interval of computation. We have demonstrated numerically in Sec. IV that solitons also can be generated in a finite trap if its size is larger than the soliton width. In this case we have observed emergence of large-amplitude dark solitons near the center of the trap (see Fig. 10). Large-amplitude bright solitons oscillating between the walls of the trap (see Fig. 13) were also generated using autoresonance with a standing wave drive. We have illustrated excitation of solitons for one special type of nonperiodic boundary conditions. The autoresonant generation of solitons and soliton trains for more general boundary conditions is an attractive goal for future studies.

In summary, we have shown that passage through Bogolubov resonance using chirped frequency space-time modulations of the interaction strength yields (if above a threshold) autoresonant synchronization between the excited growing amplitude structure and the drive. The main advantage of this promising technique is that large-amplitude solitary structures can be excited by small driving perturbations of the interaction strength if the chirp rate of the driving frequency is sufficiently small. As a result, one can adiabatically generate nearly pure solitons with predefined parameters in contrast to other methods using large perturbations (e.g., phase or density “engineering” approaches [33,34]). The autoresonance using the management of the interaction strength via Feshbach resonance opens the possibility of formation of other nonlinear coherent structures in BECs (e.g., multiphase solutions [35]),

which seems to be an important task for future research. A proximity to the Feshbach resonance may lead to increased dissipation in the chirped-driven system. It was shown previously [36,37] that a sufficiently small dissipation in other applications did not destroy the autoresonant synchronization, but modified the threshold for transition to autoresonance. The study of this effect in BECs driven by oscillating interaction strength is also an important goal for the future.

#### APPENDIX: DARK SOLITONS

We write the dark soliton solution [17] in the following form:

$$\varphi_s(x, t) = Ae^{i(\Psi + \Psi_N)}, \quad (\text{A1})$$

where in the phase

$$\Psi = -(\kappa^2 + 2U_0^2)t + \kappa x,$$

$$\Psi_N = -\tan^{-1}\{\mu \tanh[bU_0(x - Vt)]\},$$

$\mu = sb/\sqrt{1-b^2}$ ,  $s = \pm 1$ ,  $0 < b < 1$ , and the soliton shape and the velocity are

$$A = U_0\sqrt{1-b^2/\cosh^2[bU_0(x - Vt)]}, \quad (\text{A2})$$

$$V = 2\kappa + 2sU_0\sqrt{1-b^2}. \quad (\text{A3})$$

Parameter  $s$  defines the sign of the nonlinear shift of the soliton phase  $\Psi_N(-\infty) - \Psi_N(+\infty)$ .

- 
- [1] C. Chin, R. Grimm, P. Julienne, and E. Tiesinga, *Rev. Mod. Phys.* **82**, 1225 (2010).
- [2] Y. V. Kartashov, B. A. Malomed, and L. Torner, *Rev. Mod. Phys.* **83**, 247 (2011).
- [3] H. Sakaguchi and B. A. Malomed, *Phys. Rev. E* **70**, 066613 (2004).
- [4] G. Theocharis, P. Schmelcher, P. G. Kevrekidis, and D. J. Frantzeskakis, *Phys. Rev. A* **74**, 053614 (2006).
- [5] S. Holmes, M. A. Porter, P. Krüger, and P. G. Kevrekidis, *Phys. Rev. A* **88**, 033627 (2013).
- [6] F. Pinsky, N. G. Berloff, and V. M. Pérez-García, *Phys. Rev. A* **87**, 053624 (2013).
- [7] O. Gamayun, Yu. V. Bezvershenko, and V. Cheianov, *Phys. Rev. A* **91**, 031605(R) (2015).
- [8] O. V. Marchukov, B. A. Malomed, V. A. Yurovsky, M. Olshanii, V. Dunjko, and R. G. Hulet, *Phys. Rev. A* **99**, 063623 (2019).
- [9] T. Mežnaršič, R. Zitko, T. Arh, K. Gosar, E. Zupanic, and P. Jeglič, *Phys. Rev. A* **101**, 031601(R) (2020).
- [10] R. Yamazaki, S. Taie, S. Sugawa, and Y. Takahashi, *Phys. Rev. Lett.* **105**, 050405 (2010).
- [11] S. Burger, K. Bongs, S. Dettmer, W. Ertmer, K. Sengstock, A. Sanpera, G. V. Shlyapnikov, and M. Lewenstein, *Phys. Rev. Lett.* **83**, 5198 (1999).
- [12] R. Dum, J. I. Cirac, M. Lewenstein, and P. Zoller, *Phys. Rev. Lett.* **80**, 2972 (1998).
- [13] K. E. Strecker, G. B. Partridge, A. G. Truscott, and R. G. Hulet, *Nature (London)* **417**, 150 (2002).
- [14] L. Khaykovich, F. Schreck, G. Ferrari, T. Bourdel, J. Cubizolles, J. D. Carr, Y. Castin, and C. Salomon, *Science* **296**, 1290 (2002).
- [15] F. Dalfovo, S. Giorgini, L. P. Pitaevskii, and S. Stringari, *Rev. Mod. Phys.* **71**, 463 (1999).
- [16] M. J. Ablowitz and H. Segur, *Solitons and the Inverse Scattering Transform* (SIAM, Philadelphia, 1981).
- [17] Y. S. Kivshar and B. Luther-Davies, *Phys. Rep.* **298**, 81 (1998).
- [18] L. Friedland, *Scholarpedia* **4**, 5473 (2009).
- [19] A. I. Nicolin, M. H. Jensen, and R. Carretero-Gonzalez, *Phys. Rev. E* **75**, 036208 (2007).
- [20] M. Centurion, M. A. Porter, P. G. Kevrekidis, and D. Psaltis, *Phys. Rev. Lett.* **97**, 033903 (2006).
- [21] Y. Kominis and K. Hizanidis, *Opt. Express* **16**, 12124 (2008).
- [22] A. G. Shagalov and L. Friedland, *Phys. Rev. E* **106**, 024211 (2022).
- [23] G. B. Whitham, *Linear and Nonlinear Waves* (Wiley, New York, 1974).
- [24] J. Schloss, P. Barnett, R. Sachdeva, and T. Busch, *Phys. Rev. A* **102**, 043325 (2020).
- [25] C.-X. Zhu, W. Yi, G.-C. Guo, and Z.-W. Zhou, *Phys. Rev. A* **99**, 023619 (2019).
- [26] A. J. Leggett, *Rev. Mod. Phys.* **73**, 307 (2001).
- [27] L. Friedland and A. G. Shagalov, *Phys. Rev. E* **94**, 042216 (2016).
- [28] V. Zakharov and L. Ostrovsky, *Physica D* **238**, 540 (2009).

- [29] G. P. Agrawal, *Nonlinear Fiber Optics*, 4th ed. (Academic Press, San Diego, 2007), p. 121.
- [30] L. Salasnich, A. Parola, and L. Reatto, *Phys. Rev. Lett.* **91**, 080405 (2003).
- [31] L. D. Carr and J. Brand, *Phys. Rev. Lett.* **92**, 040401 (2004).
- [32] C. Wang, K. J. H. Law, P. G. Kevrekidis, and M. A. Porter, *Phys. Rev. A* **87**, 023621 (2013).
- [33] Z. Dutton, M. Budde, C. Slowe, and L. V. Hau, *Science* **293**, 663 (2001).
- [34] J. Denschlag, J. E. Simsarian, D. L. Feder, C. W. Clark, L. A. Collins, J. Cubizolles, L. Deng, E. W. Hagley, K. Helmerson, W. P. Reinhardt *et al.*, *Science* **287**, 97 (2000).
- [35] L. Friedland and A. G. Shagalov, *Phys. Rev. E* **71**, 036206 (2005).
- [36] J. Fajans, E. Gilson, and L. Friedland, *Phys. Plasmas* **8**, 423 (2001).
- [37] I. Barth, L. Friedland, E. Sarid, and A. G. Shagalov, *Phys. Rev. Lett.* **103**, 155001 (2009).